Supporting information: Correlating Lattice Distortions, Ion Migration Barriers, and Stability in Solid Electrolytes

Kwangnam Kim[†] and Donald J. Siegel[†, ‡, §, ‖, *]

[†]Mechanical Engineering Department, [‡]Materials Science & Engineering, [§]Applied Physics Program, [‖]University of Michigan Energy Institute, University of Michigan, Ann Arbor, Michigan 48109-2125, United States

*djsiege@umich.edu

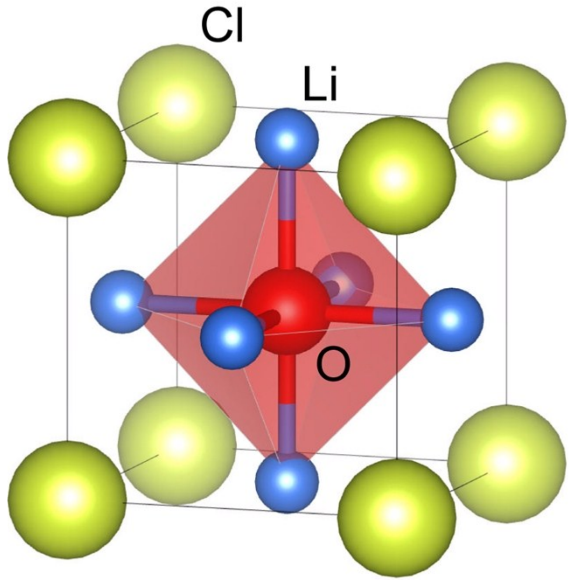

Figure S1. Unit cell of anti-perovskite Li_3OCl in the cubic Pm-3m structure. Cl ions form the cubic framework and enclose Li_6O octahedron.

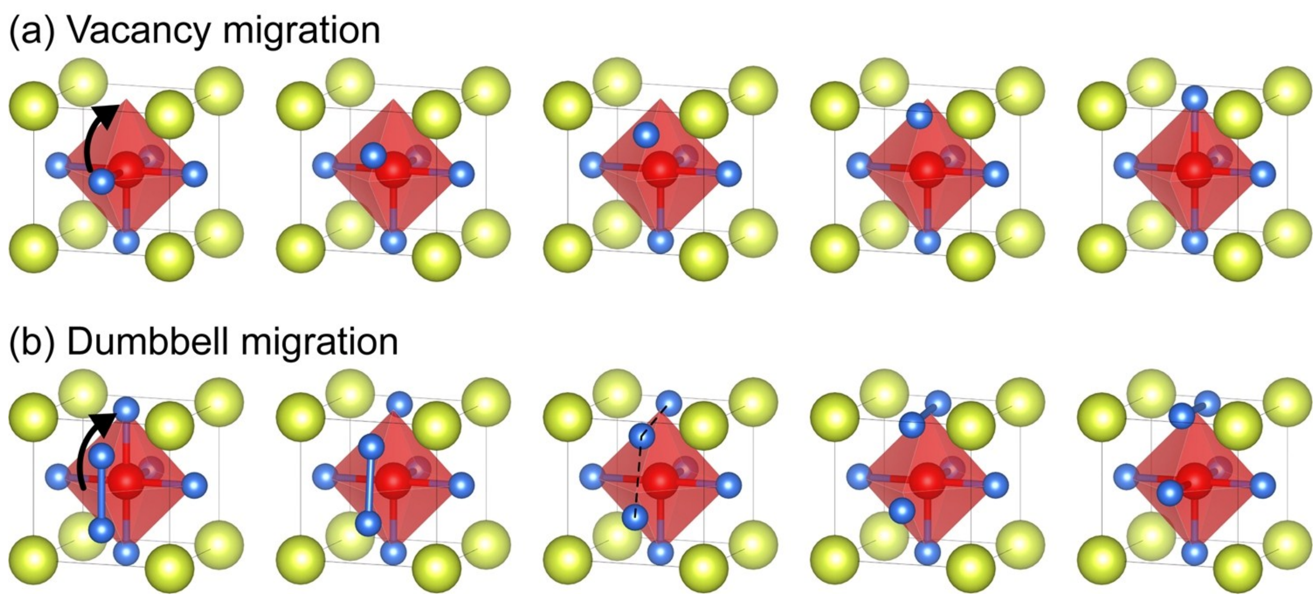

Figure S2. Migration mechanisms for (a) vacancies and (b) interstitial dumbbells.[1]

Murnaghan equation of state

Energy vs. volume data for the anti-perovskite (AP) compounds and their potential decomposition phases (i.e., chalcogenides and halides) were fit to the Murnaghan equation of state (EOS).[2]

$$E(V) = \frac{B_0 V}{B_0^{'}(B_0^{'} - 1)}\left[B_0^{'}\left(1 - \frac{V_0}{V}\right) + \left(\frac{V_0}{V}\right)^{B_0^{'}} - 1\right] + E_0$$

Here B_0 is the bulk modulus, $B_0^{'}$ is the pressure derivative of the bulk modulus, V_0 is the equilibrium volume and E_0 is the constant. The structural parameters of AP compounds and corresponding bulk moduli are listed in Table S2 and S3.

Structures of model AP compounds

Table S1 lists the tolerance factors for the anti-perovskite compounds and the calculated energies of the quasi-orthorhombic, hexagonal, and quasi-cubic structures relative to that of cubic Pm-3m structure. Compounds identified with an asterisk in identify cases where the atomic configuration underwent significant relaxations relative to the initial configuration, suggesting that the initial structure was a poor approximation. In the case of the perovskite Ia-3 structure the two cation sites are indistinguishable;[3,4] therefore, the same indistinguishability applies to the chalcogen and halogen sites in the anti-perovskite analogue. Thus, initial Ia-3 structures for the anti-perovskites were generated assuming a random distribution of chalcogen and halogen ions.

Table S1. Calculated energies (meV/atom) and tolerance factors, *t*, for 24 candidate anti-perovskite solid electrolytes. Energies are reported following structure relaxation from three initial structures: orthorhombic, hexagonal, and cubic (Ia-3). Energies are relative to the cubic (Pm-3m) structure. Values in italics indicate the energy of the most stable structure for a given composition. Values marked by an asterisk indicate that large structure changes occurred during relaxation. Compounds marked with † indicate that the halogen and chalcogen spontaneously interchange positions during relaxation; in these cases, the *t* value for the relaxed structure is also given in parentheses.

Li-based Compounds	*t*	Quasi-orthorhombic (Pnma)	Hexagonal ($P6_3cm$)	Quasi-cubic (Ia-3)
Li_3OF	0.68	-107.3	11.3	*-109.6*
Li_3OCl	0.84	*-0.6* (-0.16)[5]	105.0	45.9*
Li_3OBr	0.89	*-0.5*	120.1	47.3*
Li_3OI	0.97	-1.2	115.0	*-19.2**
Li_3SF†	0.57(0.88)	*-14.9*	154.6*	36.3*
Li_3SCl	0.70	-99.6	-0.8	*-104.1*
Li_3SBr	0.74	-47.0	34.3	*-49.0*
Li_3SI	0.81	*-9.3*	75.9	8.0
Li_3SeF†	0.54(0.93)	*-3.6*	209.7*	40.7*
Li_3SeCl	0.66	-152.8	*-161.6**	-153.2
Li_3SeBr	0.70	-87.1	1.7	*-91.7*
Li_3SeI	0.76	*-30.8*	44.5	-28.6

Na-based Compounds	*t*	Quasi-orthorhombic (Pnma)	Hexagonal ($P6_3cm$)	Quasi-cubic (Ia-3)
Na_3OF	0.69	*-144.6*	-5.3	-128.7
Na_3OCl	0.83	*-4.3*	115.9	59.0
Na_3OBr	0.87	*-1.6*	143.7	88.5*
Na_3OI	0.94	*-1.1*	162.6	91.8*
Na_3SF†	0.58(0.86)	*-14.0*	85.7*	--
Na_3SCl	0.70	*-110.7*	14.3	-94.3
Na_3SBr	0.74	*-57.9*	49.9	-38.4
Na_3SI	0.80	*-13.7*	96.5	28.1
Na_3SeF†	0.55(0.90)	*-1.8*	152.2*	77.8*
Na_3SeCl	0.67	*-157.4*	-124.7*	-134.4
Na_3SeBr	0.70	*-93.9*	18.6	-78.9
Na_3SeI	0.76	*-34.8*	65.1	-9.7

Table S2. Structural parameters for the anti-perovskites X_3AB (X = Li or Na, A = O, S or Se and B = F, Cl, Br or I). Values in parentheses represent previous experiment data.[6,7]

Compound	Symmetry	a (Å)	b (Å)	c (Å)	α (°)	β (°)	γ (°)
Li_3OF	Quasi-orthorhombic	5.038	5.112	7.178	89.999	89.999	89.999
Li_3OCl	Cubic (Pm-3m)	3.900 (3.91)					
Li_3OBr	Cubic (Pm-3m)	3.989 (4.02)					
Li_3OI	Cubic (Pm-3m)	4.161					
Li_3SF	Quasi-orthorhombic	5.571	5.527	7.849	89.998	90.000	89.992
Li_3SCl	Quasi-orthorhombic	6.276	6.321	8.932	89.994	90.008	89.991
Li_3SBr	Quasi-orthorhombic	6.440	6.499	9.191	89.998	90.004	90.010
Li_3SI	Quasi-orthorhombic	6.689	6.684	9.458	90.000	90.000	90.000
Li_3SeF	Cubic (Pm-3m)	4.011					
Li_3SeCl	Quasi-orthorhombic	6.453	6.485	9.160	90.000	89.998	90.004
Li_3SeBr	Quasi-orthorhombic	6.651	6.677	9.464	89.999	90.014	90.000
Li_3SeI	Quasi-orthorhombic	6.908	6.906	9.781	89.998	90.000	90.001
Na_3OF	Quasi-orthorhombic	5.844	6.044	8.286	89.999	89.999	89.999
Na_3OCl	Cubic (Pm-3m)	4.549 (4.491)					
Na_3OBr	Cubic (Pm-3m)	4.618 (4.564)					
Na_3OI	Cubic (Pm-3m)	4.746 (4.707)					
Na_3SF	Quasi-orthorhombic	6.312	6.269	8.918	89.998	90.002	90.001
Na_3SCl	Quasi-orthorhombic	7.045	7.157	10.013	90.002	89.999	89.995
Na_3SBr	Quasi-orthorhombic	7.190	7.345	10.264	90.024	90.067	89.993
Na_3SI	Quasi-orthorhombic	7.442	7.492	10.548	90.000	90.000	90.000
Na_3SeF	Cubic (Pm-3m)	4.509					
Na_3SeCl	Quasi-orthorhombic	7.180	7.342	10.179	90.008	89.998	89.998
Na_3SeBr	Quasi-orthorhombic	7.414	7.510	10.525	90.007	90.004	90.009
Na_3SeI	Quasi-orthorhombic	7.625	7.744	10.852	90.000	90.000	90.000

Band gap calculation

The electrochemical stability of solid electrolytes is important for the performance of batteries. The electrochemical potentials of the anode and cathode should be located within the electrochemical window of the electrolyte to prevent reduction and/or oxidation of the electrolyte.[8] The band gap of the electrolyte gives the upper limit of the battery voltage. Thus, large band gaps are desirable. Previous DFT studies predicted the band gaps of Li_3OCl and Li_3OBr (6.39 and 5.84 eV, respectively) using hybrid functionals.[9] Although hybrid functionals are more accurate than local (LDA) or semi-local (GGA) functionals, in general they underestimate band gaps.[10]

To provide a more accurate estimate of the bandgaps of the anti-perovskite compounds examined here, two variants of GW method were employed: (*i.*) the 'single-shot' G_0W_0, with input wavefunctions evaluated with the HSE06 hybrid functional[11,12], and (*ii.*) the partially self-consistent GW_0 method, which uses wavefunctions evaluated from a prior PBE calculation. In the GW_0 approach the eigenvalues are updated, while the wavefunctions are kept fixed. These two GW variants have yielded very good agreement with experimental band gaps.[10,13] Both calculations used 1024 bands and 64 frequency points; 4 iterations were performed in the GW_0 calculations. Test calculations with larger values for these parameters showed no significant change to the band gaps.

The band gaps of Li/Na anti-perovskites predicted by these GW methods are summarized in Table S3. The G_0W_0 method with HSE06 hybrid functional input wavefunctions gives slightly larger band gaps than the GW_0-GGA method. Generally, the band gaps are smaller for those compounds containing larger halogens and chalcogens. The lithium-based compounds have band gaps of 6 eV or larger, while the sodium-based systems have gaps in the range of 4 – 5 eV.

Table S3. Predicted bulk moduli and band gaps of anti-perovskite compounds. Values in parentheses represent previous DFT predictions.[14]

Li-based Compound	Bulk modulus (GPa)	Band gap (eV)		Na-based Compound	Bulk modulus (GPa)	Band gap (eV)	
		G_0W_0@HSE06	GW_0@GGA			G_0W_0@HSE06	GW_0@GGA
Li_3OF	59.7	8.64	8.37	**Na_3OF**	36.8	4.92	4.66
Li_3OCl	52.9 (55.7)	8.07	7.89	**Na_3OCl**	32.4 (36.4)	5.08	4.94
Li_3OBr	48.6 (52.3)	7.30	7.10	**Na_3OBr**	31.2 (34.0)	4.64	4.47
Li_3OI	43.4	6.38	6.21	**Na_3OI**	28.9	4.41	4.31
Li_3SF	43.2	7.08	6.86	**Na_3SF**	31.8	5.16	5.06
Li_3SCl	29.7	6.75	6.58	**Na_3SCl**	21.6	4.98	4.89
Li_3SBr	28.8	6.36	6.18	**Na_3SBr**	21.0	4.84	4.72
Li_3SI	27.7	5.67	5.52	**Na_3SI**	20.0	4.74	4.65
Li_3SeF	47.5	6.08	5.87	**Na_3SeF**	34.2	4.59	4.52
Li_3SeCl	25.4	5.93	5.78	**Na_3SeCl**	18.3	4.43	4.35
Li_3SeBr	24.7	5.75	5.59	**Na_3SeBr**	18.3	4.42	4.33
Li_3SeI	24.0	5.42	5.28	**Na_3SeI**	17.6	4.39	4.31

‘F-centered’ compounds

During relaxation of the F-based compounds Li_3SF, Li_3SeF, Na_3SF, and Na_3SeF, the chalcogen and halogen ions spontaneously interchange positions via rearrangement of the Li-ion sublattice (Fig. S3). The initial structures of these compounds have very low tolerance factors, $t < 0.6$, due to the small ionic radius of F. As discussed elsewhere,[15-17] a lower tolerance factor correlates with lower stability, thus a structure change resulting from instabilities is not unexpected. The observed rearrangements partially remedy the instability, as the interchanged compounds exhibit much higher tolerance factors, $t > 0.86$. The resulting low-energy structures are quasi-orthorhombic. Li_3SeF and Na_3SeF are treated as cubic Pm-3m (Group 1), however, due to the negligible energy differences (< 4 meV/atom) between the cubic and quasi-orthorhombic structures. Li_3SF and Na_3SF have moderately distorted structures, placing them in Group 2.

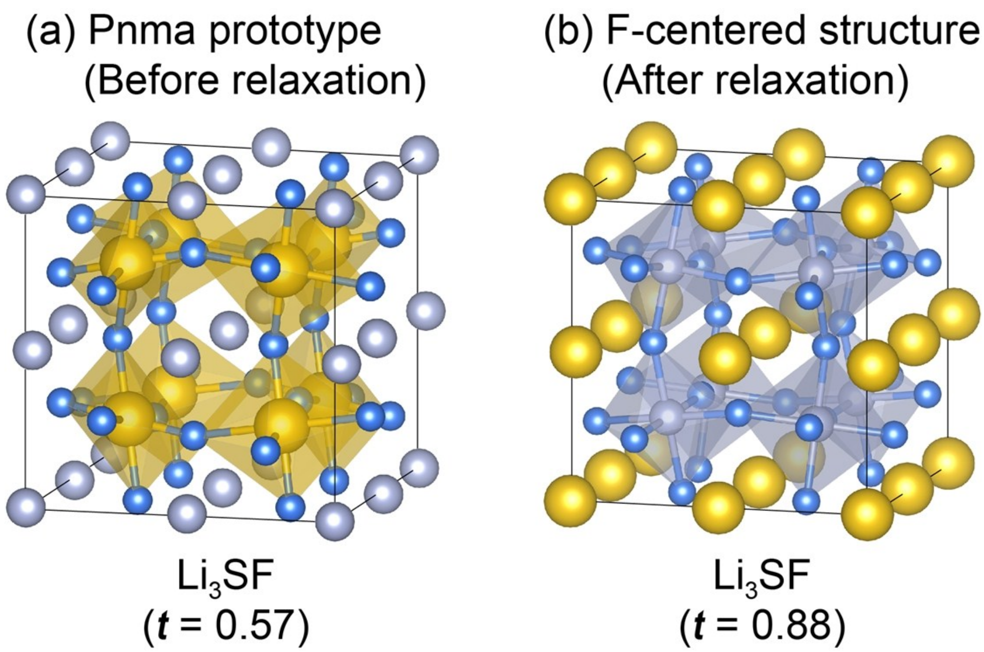

Figure S3. An example of an F-centered structure, Li_3SF. (a) The structure before relaxation based on the Pnma prototype ($CaTiO_3$). (b) Structure after relaxation and interchange of S and F. The Li ions (blue) are situated at the octahedra vertices with F ions (grey) at the octahedra center. S-ions (yellow) occupy the framework positions.

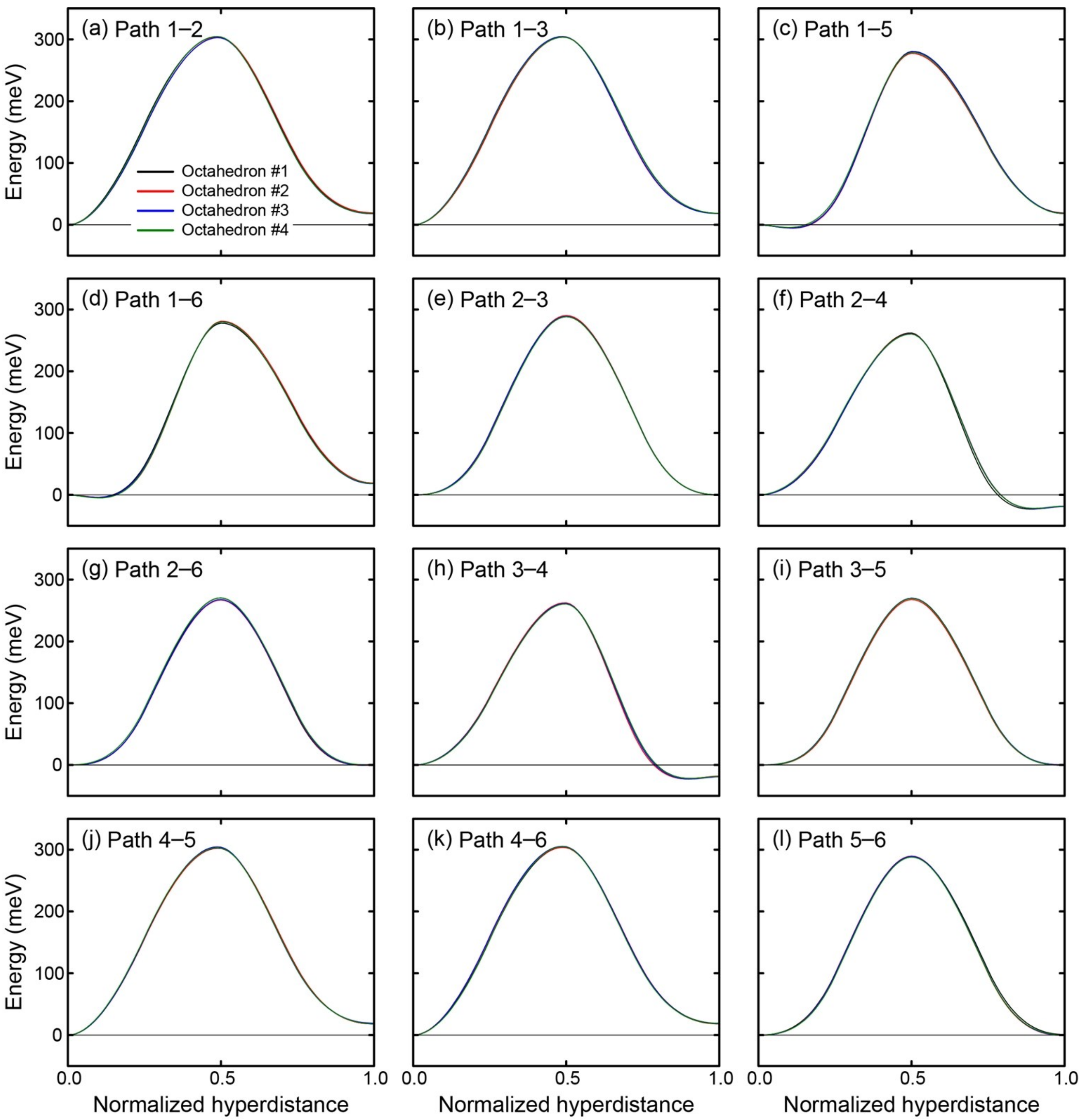

Figure S4. Comparison of elementary vacancy migration barriers evaluated for the 12 possible migration paths on the 4 distinct octahedra in Li_3SI. This compound was selected as a test case as it has the largest structural differences between the 4 octahedra. Hopping paths are labelled according to the cation position, as shown in Fig. 2. Octahedra 1 – 4 are also shown in Fig. 2, starting from the bottom-right octahedron and progressing clockwise. The data show that the difference in hopping barriers on distinct octahedra is negligible.

Example of migration pathway construction

Long-range ion migration pathways were constructed by combining adjacent elementary hopping events. Here, and in Fig. S5, we describe the procedure for assembling these long-range pathways. (a.) A specific site is selected as an initial position for a vacancy or interstitial (marked as black circle). For demonstration purposes site 4 on the green (bottom-right) octahedron is chosen. (b.) This defect can potentially migrate to positions 2, 3, 5 and 6 on the same octahedron and to positions 2, 3, 5, and 6 on the orange octahedron above. Path 4 → 6 on the green octahedron is selected as it has the lowest barrier (53 meV) among the 8 available paths (black arrow). (c.) At the new site there are 7 available paths: 3 paths to positions 1, 2, and 5 on the green octahedron (reversing to position 4 is prohibited), and 4 paths in another octahedron (not shown) by following the connection 6 = 5. The path 6 → 1 in the green octahedron has the lowest barrier (112 meV) among these 7 paths. However, among the 7 discarded paths in the previous step, the barrier of path 1 → 6 (red arrow) is 70 meV, which is lower than the 112 meV barrier in the current step. Thus, the search reverts to the previous step and selects the next lowest barrier, path 1 → 6, into the orange octahedron. (d.) Repeat step 3. At the current step, there are 7 available non-reversing paths: 3 paths to positions 2, 4, and 5 in the orange octahedron, and 4 paths in another octahedron (not shown) by following the connection 6 = 5. The path into position 4 in the top-right octahedron (6 → 4, blue arrow) has the lowest barrier (95 meV). This barrier is smaller than any other path discarded previously, thus the defect continues along this path. Due to the connection 4 = 1, the defect has arrived at a site equivalent to the initial site via pathway 1 → 6 → 4 (= 1). This pathway has a limiting barrier = 95 meV. (e.) Return to step (a.) and repeat steps (a.) to (d.) to examine pathways starting from all other initial positions. This procedure identifies the pathway that has the "smallest maximum" barrier, referred to as the *limiting barrier*; this pathway will be the most likely pathway to contribute to macroscopic ion migration.

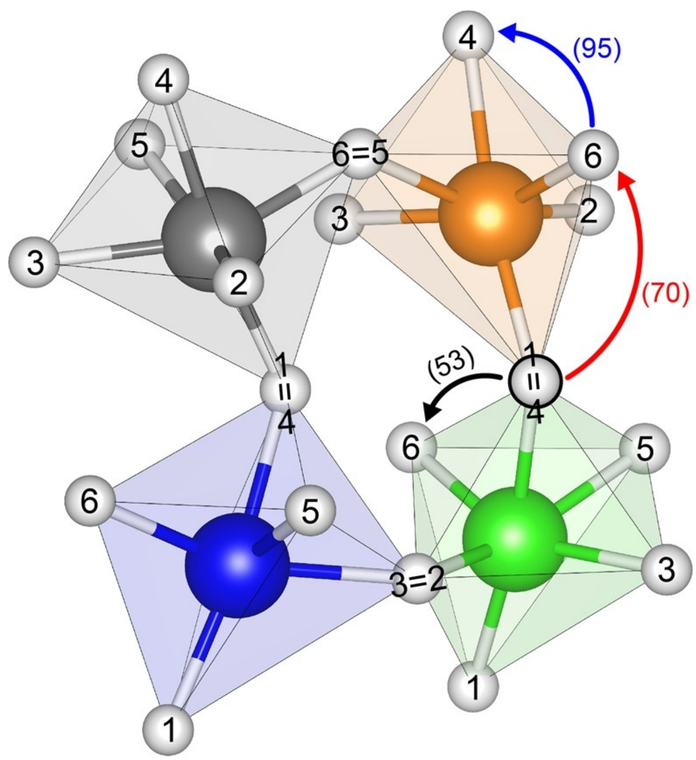

Figure S5. Example of the procedure used to identify percolating pathways for vacancy migration in Na_3SeCl. Values in parentheses are activation energy barriers (in meV) for elementary hops between sites connected by arrows. The site circled in black (1=4) is the starting point for the pathway.

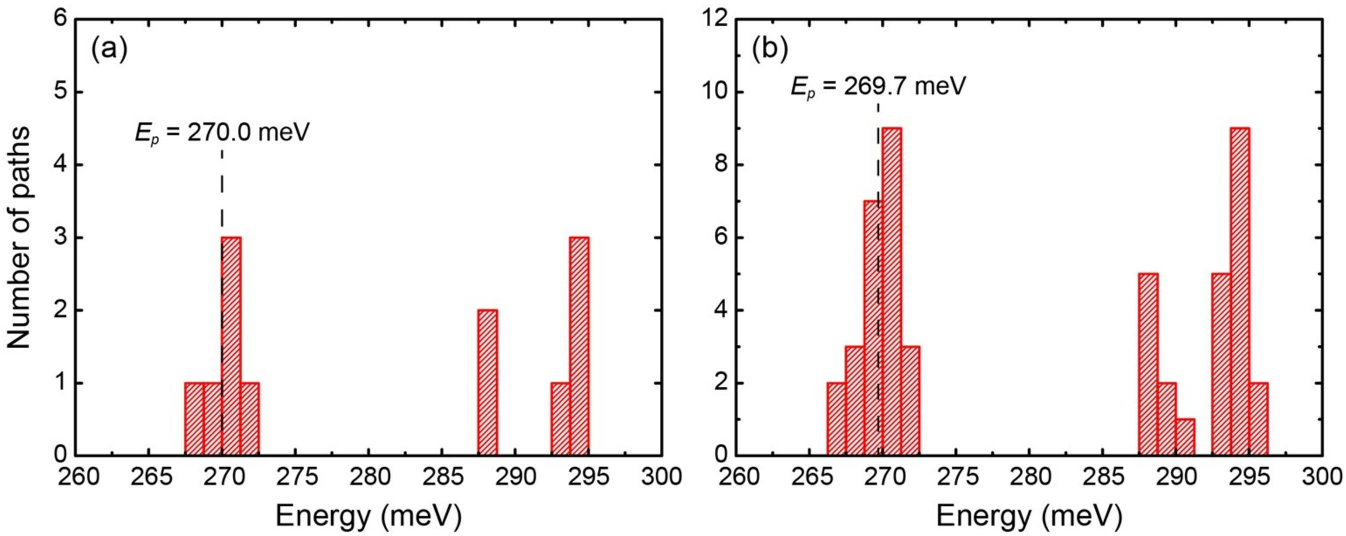

Figure S6. Histograms of the elementary barrier energies for vacancy migration in Li_3SI. (a) 12 barriers that orbit a single octahedron. Using the bond percolation threshold p = 0.18, the values for k and d (see main text) are 2 and 0.36, respectively. The effective energy barrier E_p = 270.0 meV. (b) Histogram constructed from 48 barriers from all four distinct octahedra in Li_3SI. In this case E_p = 269.7 meV. Thus, mapping of hopping barriers on a single octahedron yields very similar results to that from a more comprehensive sampling of multiple octahedra.

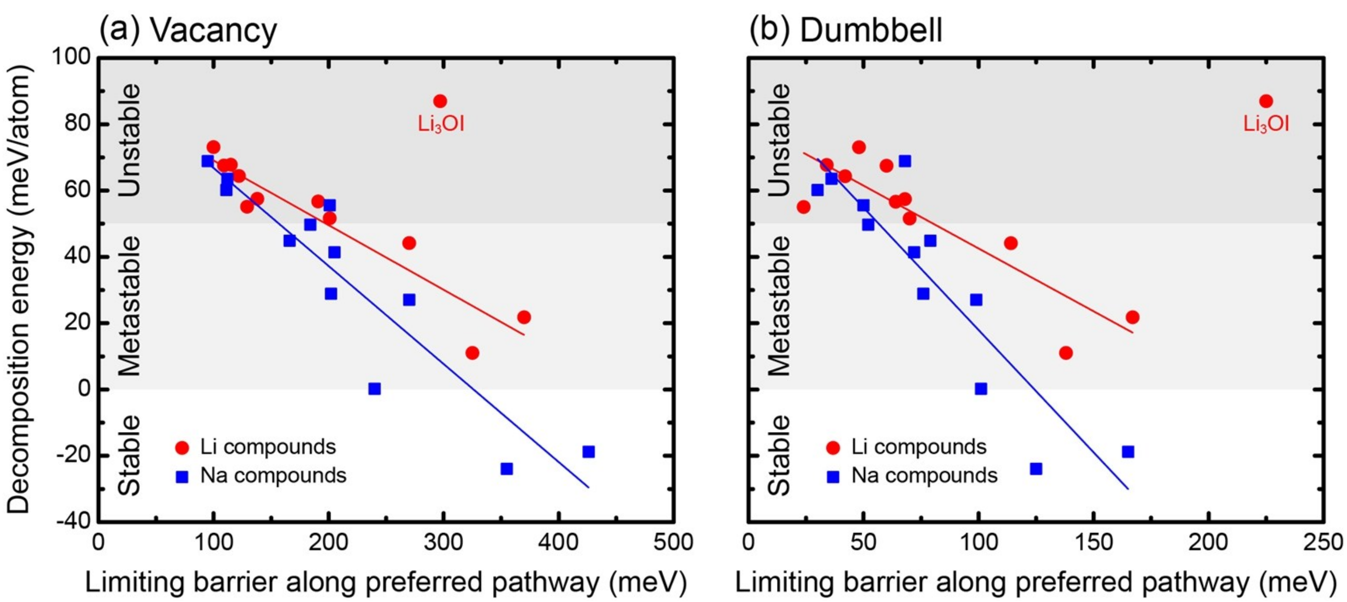

Figure S7. Correlation between the limiting barrier and the decomposition energy, E_d for (a) vacancy (Pearson correlation coefficients are -0.94 and -0.92 for Li and Na compounds, respectively, excluding the Li_3OI outlier) and (b) interstitial dumbbell migrations (Pearson correlation coefficients are -0.88 and -0.90 for Li and Na compounds, respectively, excluding the Li_3OI outlier).

Thermodynamic stability

Previous DFT studies[1,9] have predicted the thermodynamic stability of Li_3OCl (LOC) and Li_3OBr (LOB) and suggested that these compounds are unstable at 0 K with respect to decomposition into Li_2O and LiCl or LiBr. For these compounds the calculated decomposition energies were 13.9 and 25.8 meV/atom, respectively.[9] Taking a similar approach, here we assume that the anti-perovskite compositions considered here are also located on the tie line between a Li/Na chalcogenide and a halide. Figure 6 plots the decomposition energies, E_d, of the anti-perovskites (i.e., the energy relative to the convex hull) as a function of the tolerance factor, t. The data indicates that the tolerance factor and E_d are correlated; the compounds with higher degrees of distortion tend to be more unstable.

It is important to note that a positive value for E_d at zero Kelvin does not guarantee that a given compound will be impossible to synthesized.[18,19] For example, despite having $E_d > 0$, many experimental studies have successfully synthesized LOC and LOB.[6,20-23] Possible explanations for this discrepancy include: inaccuracies in DFT, finite temperature effects, and kinetic stabilization.[9,18,19,24] Previous studies assessed the accuracy of DFT by comparing calculated energies to experimental data.[25,26] Hautier et al. estimated the formation energies of ternary oxides and found that 90% of the errors are within ± 40 meV/atom (standard deviation = 24 meV/atom).[25] Also, among 736 compounds extracted from the ICSD with composition ABX_3, 59% are predicted to be stable at 0 K, 26% are within 50 meV/atom above the hull, and 10% are between 50 – 150 meV/atom.[26] Following literature precedent,[26] the anti-perovskites were grouped into three categories based on their decomposition energies: (*i.*) Stable, $E_d < 0$, (*ii.*) Metastable, E_d within 0 – 50 meV/atom, and (*iii.*) unstable, $E_d > 50$ meV/atom. 11 compounds have $E_d < 50$ meV, Table S4.

Furthermore, compounds above the convex hull at 0 K could be stabilized under other conditions.[18] For example, LOC could be stabilized by vibrational entropy at high temperatures,[5] such as those encountered during synthesis.[6] Contributions to vibrational entropy arise from softer/longer Li – Cl bonds in LOC than in LiCl, and from additional octahedron rotational modes.[5,27] Following Chen et al.,[5] these bond length differences can be defined as $\Delta\delta = \overline{\delta}_{AP} - \delta_{Halide\ or\ chalcogenide}$, where $\overline{\delta}_{AP}$ is the average length of bonds between Li/Na and the framework anion in an anti-perovskite. $\delta_{Halide\ or\ chalcogenide}$ is the bond length in the relevant halide or chalcogenide (depending on the type of framework anion in the anti-perovskite). Figure S8 shows that a strong linear correlation exists between the tolerance factor and the bond length difference: larger distortions result in larger differences in bond lengths. Thus, we anticipate that compounds with larger distortions of the octahedra will gain more vibrational entropy due to bond softening. Therefore, the APs would be stabilized at elevated temperatures if the entropy effect overcomes the energy above convex hull. Li_3OI is an outlier to this trend: despite having the most ordered structure ($t = 0.97$), it has the most positive E_d. Since its average Li – I bond is stronger (shorter) than that in LiI, stabilization via entropy is not likely.

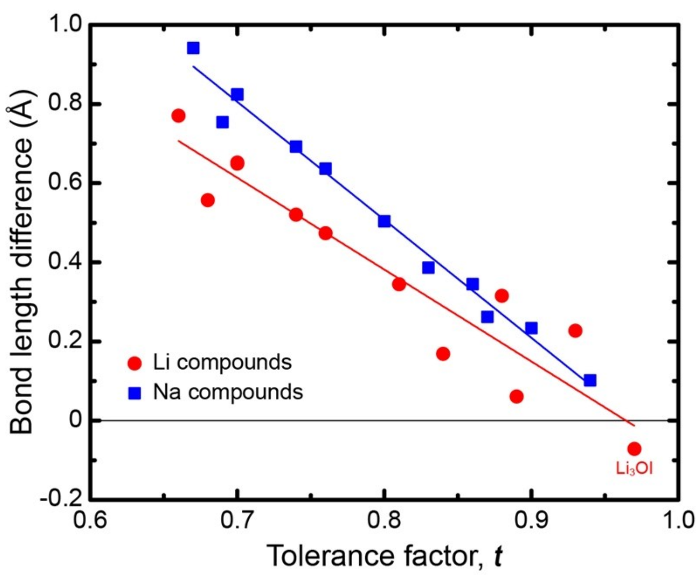

Figure S8. Correlation between the bond length difference, $\Delta\delta$ (as described above), and the tolerance factor. Pearson correlation coefficients are -0.94 and -0.99 for Li and Na compounds, respectively.

Table S4. Calculated decomposition energies, E_d, of the anti-perovskites at zero Kelvin. Positive values imply that decomposition into a mixture of chalcogenide and halide is favored. Values in parentheses represent previous DFT predictions.[9]

Li-based Compounds	E_d (meV/atom)	Na-based Compounds	E_d (meV/atom)
Li_3OF	55.1	**Na_3OF**	55.6
Li_3OCl	11.1 (13.9)	**Na_3OCl**	0.2
Li_3OBr	21.9 (25.8)	**Na_3OBr**	-23.9
Li_3OI	87.0	**Na_3OI**	-18.7
Li_3SF	67.6	**Na_3SF**	44.9
Li_3SCl	67.7	**Na_3SCl**	63.6
Li_3SBr	56.7	**Na_3SBr**	49.7
Li_3SI	44.1	**Na_3SI**	27.1
Li_3SeF	57.5	**Na_3SeF**	28.9
Li_3SeCl	73.1	**Na_3SeCl**	68.9
Li_3SeBr	64.3	**Na_3SeBr**	60.2
Li_3SeI	51.6	**Na_3SeI**	41.4

Path width

The diameter of the migration pathway traversed by a migrating vacancy or interstitial was measured as follows: (1) First, identify adjacent ions whose positions fall between the path's endpoints. (2) Measure the perpendicular distance of these ions to the vector describing the ion migration path. These distances account for the ionic radius, and involve the first and second nearest neighbors. (3) Also, because three Li-ions are involved in the dumbbell mechanism, three different path widths are obtained. We selected the narrowest width among these cases. A detailed explanation of the perpendicular distance algorithm can be found in Ref. 28.

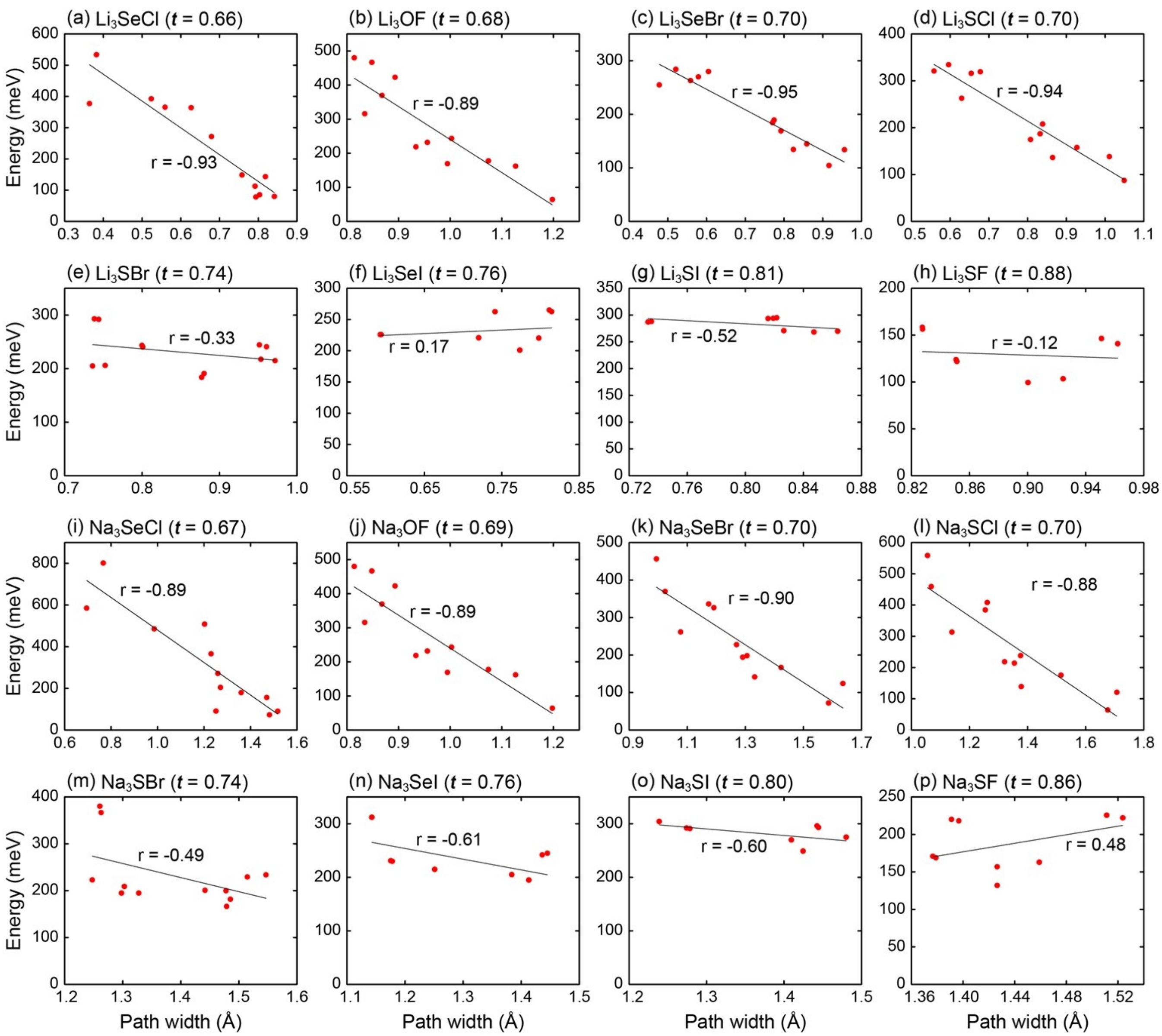

Figure S9. Correlation between path width and elementary barrier energies for vacancy migration in the distorted (a-h) lithium and (i-p) sodium anti-perovskites. r values represent Pearson correlation coefficients. The Goldschmidt tolerance factor, t, is also given for each compound; graphs are ordered based on t.

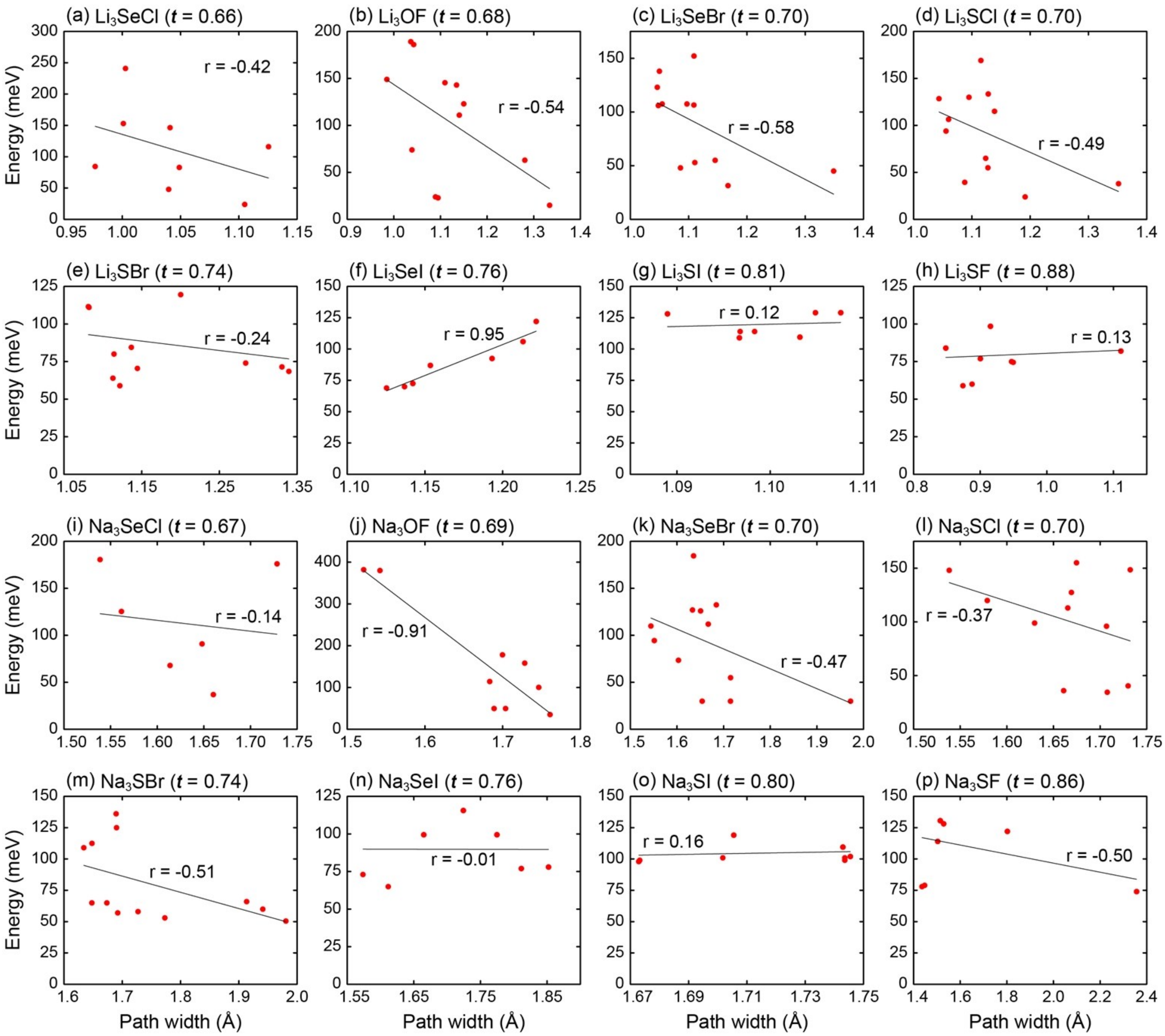

Figure S10. Correlation between path width and elementary barrier energies for interstitial dumbbell migration in the distorted (a-h) lithium and (i-p) sodium anti-perovskites. r values represent Pearson correlation coefficients. The Goldschmidt tolerance factor, t, is also given for each compound; graphs are ordered based on t.

REFERENCES

(1) Emly, A.; Kioupakis, E.; Van der Ven, A. Phase Stability and Transport Mechanisms in Antiperovskite Li_3OCl and Li_3OBr Superionic Conductors. *Chem. Mater.* **2013**, *25* (23), 4663-4670.

(2) Murnaghan, F. D. The Compressibility of Media under Extreme Pressures. *Proc. Natl. Acad. Sci. U. S. A*. **1944**, *30* (9), 244-247.

(3) Alonso, J. A.; Casais, M. T.; Mart'inez-Lope, M. J. Preparation and Topotactical Oxidation of $ScVO_3$ with Bixbyte Structure: A Low-Temperature Route to Stabilize the New Defect Fluorite $ScVO_{3.5}$ Metastable Phase. *Dalt. Trans.* **2004**, *0* (9), 1294–1297.

(4) Bréard, Y.; Fjellvåg, H.; Hauback, B. Investigation of Bixbyite Type Scandium Oxides Involving a Magnetic Cation: $Sc_{2-x}Fe_xO_3$ ($0 \leq x \leq 1$). *Solid State Commun.* **2011**, *151* (3), 223–226.

(5) Chen, M-H.; Emly, A.; Van der Ven, A. Anharmonicity and phase stability of antiperovskite Li_3OCl. *Phys. Rev. B: Condens. Matter Mater. Phys.* **2015**, *91* (21), 214306.

(6) Zhao, Y.; Daemen, L. L. Superionic Conductivity in Lithium-Rich Anti-Perovskites. *J. Am. Chem. Soc.* **2012**, *134* (36), 15042-15047.

(7) Wang, Y.; Wang, Q.; Liu, Z.; Zhou, Z.; Li, S.; Zhu, J.; Zou, R.; Wang, Y.; Lin, J.; Zhao, Y. Structural manipulation approaches towards enhanced sodium ionic conductivity in Na-rich antiperovskites. *J. Power Sources* **2015**, *293*, 735-740.

(8) Goodenough, J. B.; Kim, Y. Challenges for Rechargeable Li Batteries. *Chem. Mater.* **2011**, *22* (3), 587-603.

(9) Zhang, Y.; Zhao, Y; Chen, C. *Ab initio* study of the stabilities of and mechanism of superionic transport in lithium-rich antiperovskites. *Phys. Rev. B: Condens. Matter Mater. Phys.* **2013**, *87* (13), 134303.

(10) Shishkin, M.; Kresse, G. Self-consistent GW calculations for semiconductors and insulators. *Phys. Rev. B: Condens. Matter Mater. Phys.* **2007**, *75* (23), 235102.

(11) Heyd, J.; Scuseria, G. E.; Ernzerhof, M. Hybrid Functionals Based on a Screened Coulomb Potential. *J. Chem. Phys.* **2003**, *118* (18), 8207–8215.

(12) Krukau, A. V.; Vydrov, O. A.; Izmaylov, A. F.; Scuseria, G. E. Influence of the Exchange Screening Parameter on the Performance of Screened Hybrid Functionals. *J. Chem. Phys.* **2006**, *125* (22), 224106.

(13) Fuchs, F.; Furthmüller, J.; Bechstedt, F.; Shishkin, M.; Kresse, G. Quasiparticle Band Structure Based on a Generalized Kohn-Sham Scheme. *Phys. Rev. B - Condens. Matter Mater. Phys.* **2007**, *76* (11), 115109.

(14) Deng, Z.; Wang, Z.; Chu, I-H.; Luo, J.; Ong, S. P. Elastic Properties of Alkali Superionic Conductor Electrolytes from First Principles Claculations. *J. Electrochem. Soc. 2*016, *163* (2), A67-A74.

(15) Yokokawa, H.; Sakai, N.; Kawada, T.; Dokiya, M. Thermodynamic Stabilities of Perovskite Oxides for Electrodes and Other Electrochemical Materials. *Solid State Ionics* **1992**, *52* (1–3), 43–56.

(16) Kreuer, K. . On the Development of Proton Conducting Materials for Technological Applications. *Solid State Ionics* **1997**, *97* (1–4), 1–15.

(17) Nagabhushana, G. P.; Shivaramaiah, R.; Navrotsky, A. Direct Calorimetric Verification of Thermodynamic Instability of Lead Halide Hybrid Perovskites. *Proc. Natl. Acad. Sci.* **2016**, *113* (28), 7717–7721.

(18) Hautier, G.; Jain, A.; Ong, S. P.; Kang, B.; Moore, C.; Doe, R.; Ceder, G. Phosphates as Lithium-Ion Battery Cathodes: An Evaluation Based on High-Throughput *ab Initio* Calculations. *Chem. Mater.* **2011**, *23* (15), 3495-3508.

(19) Armiento, R.; Kozinsky, B.; Hautier, G.; Fornari, M.; Ceder, G. High-throughput screening of perovskite alloys for piezoelectric performance and thermodynamic stability. *Phys. Rev. B: Condens. Matter Mater. Phys.* **2014**, *89* (13), 134103.

(20) Zhang, J.; Han, J.; Zhu, J.; Lin, Z.; Braga, M. H.; Daemen, L. L.; Wang, L.; Zhao, Y. High pressure-high temperature synthesis of lithium-rich $Li_3O(Cl, Br)$ and $Li_{3-x}Ca_{x/2}OCl$ anti-perovskite halides. *Inorg. Chem. Commun.* **2014**, *48*, 140-143.

(21) Lü, X.; Wu, G.; Howard, J. W.; Chen, A.; Zhao Y.; Daemen, L. L.; Jia, Q. Li-rich anti-perovskite Li_3OCl films with enhanced ionic conductivity. *Chem. Commun.* **2014**, *50* (78), 11520-11522.

(22) Li, S.; Zhu, J.; Wang, Y.; Howard, J. W.; Lü, X.; Li, Y.; Kumar, R. S.; Wang, L.; Daemen, L. L.; Zhao, Y. Reaction mechanism studies towards effective fabrication of lithium-rich anti-perovskites Li_3OX (X = Cl, Br). *Solid State Ionics* **2016**, *284*, 14-19.

(23) Lü, X.; Howard, J. W.; Chen, A.; Zhu, J.; Li, S.; Wu, G.; Dowden, P.; Xu, H.; Zhao, Y.; Jia, Q. Antiperovskite Li_3OCl Superionic Conductor Films for Solid-State Li-Ion Batteries. *Adv. Sci.* **2016**, *3* (3), 1500359.

(24) Fan, Z. Y.; Hinks, D. G.; Newman, N.; Rowell, J. M. Experimental study of MgB_2 decomposition. *Appl. Phys. Lett.* **2001**, *79* (87), 87-89.

(25) Hautier, G.; Ong, S. P.; Jain, A.; Moore, C. J.; Ceder, G. Accuracy of density functional theory in predicting formation energies of ternary oxides from binary oxides and its implication on phase stability. *Phys. Rev. B: Condens. Matter Mater. Phys.* **2012**, *85* (15), 155208.

(26) Schmidt, J.; Shi, J.; Borlido, P.; Chen, L.; Botti, S.; Marques, M. A. L. Predicting the Thermodynamic Stability of Solids Conbining Density Functional Theory and Machine Leaning. *Chem. Mater.* **2017**, *29* (12), 5090-5103.

(27) Van de Walle, A; Ceder, G. The effect of lattice vibrations on substitutional alloy thermodynamics. *Rev. Mod. Phys*. 2002, *74* (1), 11-45.

(28) Sendek, A. D.; Yang, Q.; Cubuk, E. D.; Duerloo, K.-A. N.; Cui, Y.; Reed, E. J. Holistic Computational Structure Screening of More than 12 000 Candidates for Solid Lithium-Ion Conductor Materials. *Energy Environ. Sci.* **2017**, *10* (1), 306–320.